How to cite: *Angew. Chem. Int. Ed.* **2024**, e202419992
doi.org/10.1002/anie.202419992

VIP Organic Materials Very Important Paper

Single Crystalline, Non-Stoichiometric Hydrogen-Bonded Organic Frameworks Showing Versatile Fluorescence Depending on Composition Ratios and Distributions

Taito Hashimoto[#], Mario de la Hoz Tomás[#], Ryusei Oketani, Boiko Cohen, Miki Naruoka, Norimitsu Tohnai, Abderrazzak Douhal, and Ichiro Hisaki**

Abstract: Hydrogen-bonded organic frameworks (HOFs) composed of multicomponent molecules in a non-stoichiometric composition have drawn great interest due to their tunable properties. However, the photobehavior of the single crystals of such mixed HOFs has not been explored. Here, we report on the synthesis, characterization and photobehavior of single crystalline non-stoichiometric HOFs (NS-HOFs). NS-HOFs (**B_TN_T-1**) with various composition ratios were successfully obtained as single crystals from two analogue tetratopic carboxylic acids, possessing naphthalene and benzothiadiazole cores (**NTTA** and **BTTA**, respectively). The heterogeneous distribution of the components was thoroughly confirmed by time-resolved fluorescence microscopy and local crystallographic analysis using focused synchrotron X-ray radiation. The versatile fluorescence of **B_TN_T-1** behavior depends on the composition ratio and distribution of the component in the single crystals. We observed not only fluorescence bands with various colors such as purple, blue, green and white, depending on the composition ratios, but also different emission bands from a single crystal. We provide details on their emission lifetimes following the composition, emission color and targeted region on the crystal. This work is the first example of single crystal studies applied to organic porous co-crystals and demonstrates unique and versatile optical properties of carboxylic acid-based NS-HOFs. The results provide a concept of creating functional mixed porous materials capable of different and tunable optical properties.

Introduction

Non-stoichiometric co-crystalline frameworks, in which multi components are mixed in various ratios to yield crystalline materials, have gained much attention because their physico-chemical properties can be modulated by the composition ratio of the molecular components in the framework, and moreover, new functions can emerge.[1–5] Such mixed frameworks have been actively studied in metal–organic frameworks (MOFs).[6–9] In 2010, Yaghi and co-workers reported on the first non-stoichiometric MOFs using eight kinds of *p*-phenylene ligands with different functional groups, and demonstrated that the multi-component MOFs showed higher selective uptake of CO_2 over CO than their single MOF components.[10] Recently, several research groups have reported that mixed MOFs constructed with donor-acceptor linkers in non-stoichiometric ratios can tune/enhance the luminescent and electronic functions by energy transfer between the two ligands in the framework.[11–16] Mixed covalent organic frameworks (COFs) are also reported.[19–22] Functionality such as selective gas soption[21,22] and drug release capacities[20] was tuned and improved by introducing multi-functional groups on pore surfaces of 3D COFs.

In the case of hydrogen-bonded organic frameworks (HOFs),[23–28] constructed by assembling molecules through reversible hydrogen (H) bonds, only a few non-stoichiometric HOFs (NS-HOFs) have been reported.[29,30] This may be because H-bonding is highly reversible, and therefore, the thermodynamically more favorable monocomponent or stoichiometrically-mixed frameworks tend to form rather than nonstoichiometric ones. As a representative example of NS-HOFs, Xue and co-workers reported a fluorescent two-component HOF formed from dumbbell-shaped terphenyl

[*] T. Hashimoto,[#] Dr. R. Oketani, Prof. Dr. I. Hisaki
Division of Chemistry, Graduate School of Engineering Science
Osaka University
1-3 Machikaneyama, Toyonaka, Osaka 560-8531, Japan
E-mail: i.hisaki.es@osaka-u.ac.jp
M. d. l. Hoz Tomás,[#] Prof. Dr. B. Cohen, Prof. Dr. A. Douhal
Departamento de Química Física, Facultad de Ciencias Ambientales y Bioquímica, and INAMOL
Universidad de Castilla-La Mancha
Avenida Carlos III, Toledo, 45071, Spain
E-mail: abderrazzak.douhal@uclm.es
M. Naruoka, Prof. Dr. N. Tohnai
Department of Applied Chemistry, Graduate School of Engineering
Osaka University
2-1 Yamadaoka, Suita, Osaka 565-0871, Japan
[#] These authors contributed equally.

and diphenylbenzothiadiazole derivatives.[31] In this system, the fluorescence color of bulk crystalline samples can be modulated by their composition ratios. However, the precise crystallographic analysis using single crystals has not been conducted presumably because of problems on their crystallinity or size of single crystals. Constructing single crystals of NS-HOFs with enough size for single crystalline X-ray diffraction (SCXRD) analysis remains a significant challenge.

Faced with this challenge, we have recently succeeded in preparing single crystalline NS-HOFs, in which two analogues tetrakis(carboxyphenyl) pyrene and 1,2,3,6,7,8-hydropyrene derivatives are coexistent to form ***sql***-topological network sheets through intermolecular H-bonding of carboxy groups.[32] SCXRD analysis revealed their precise structures, whose cell parameters varied in proportion to the composition ratio that nearly corresponds to that in the initial solutions. Furthermore, macroscopic Raman spectroscopy on a single crystal revealed that the distribution of the components was not homogeneous. Recently, Chen and coworkers also prepared NS-HOFs based on tetrakis(4-carboxyphenyl)pyrene derivatives bearing –H, $–CH_3$, $–NH_2$ and –F groups, solved their crystal structure by SCXRD, and demonstrated that the hydrophobicity of the HOFs can be modulated depending on the components fraction.[30] These reports demonstrate that a certain carboxylic acid can form a single crystalline NS-HOF, making it possible to conduct precise crystallographic analysis necessary for establishing the design principle of NS-HOFs.

In this study, we prepared new NS-HOFs using benzothiadiazole (BT) and naphthalene (NT) chromophores with different fluorescence properties because of the following two reasons: (1) Accurate distribution of the components can be revealed by fluorescence mapping, and (2) rich optical properties such as color-tunable emission and/or dual color emission can be achieved from single crystals (Figure 1). We applied two tetratopic carboxylic acids possessing a BT and NT core (**BTTA** and **NTTA**, respectively) as building block molecules of the NS-HOF, since they have closely similar molecular shapes, while showing different fluorescence colors. Indeed, these two compounds yielded NS-HOFs, $\mathbf{B_TN_T}$**-1**, with various composition ratios. The single crystals of $\mathbf{B_TN_T}$**-1** exhibit fluorescence with different colors such as purple, blue, green and white, depending on the composition ratio. More interestingly, dual fluorescence was also observed from the single crystals due to non-uniform distribution of the components. The local crystal structures and photophysical properties of the single crystals with the heterogeneous distribution were thoroughly investigated by focused synchrotron X-ray radiation technique and time-resolved fluorescence microscopy, respectively. These works are the first examples of essential single crystal study to reveal the composition- and distribution-dependent fluorescence of NS-HOF single crystals and give new insights for the development of functional fluorescent porous materials.

Results and Discussion

Crystallography of Mono-Component HOFs of BTTA and NTTA

5',5''-[Benzo[*c*][1,2,5]thiadiazole-4,7-diyl)bis([1,1':3',1''-terphenyl]-4,4''-dicarboxylic acid)] (**BTTA**) and 5',5'''-[naphthalene-1,4-diylbis([1,1':3',1''-terphenyl]-4,4''-dicarboxylic acid)] (**NTTA**) were synthesized according to literature.[33,34] **BTTA** was recrystallized from a mixed solution of *N*,*N*-dimethylformamide (DMF) and 1,2,4-trichlorobenzene (TCB) at 100 °C to give HOF **BTTA-1** as we reported previously.[33] Figure S1 and Table S1 show the crystal structure and data of **BTTA-1**, respectively, as a reference. **NTTA** was recrystallized by slow evaporation of a mixed solution of DMF and TCB at 60 °C to give HOF **NTTA-1** as plate shape crystals, suitable for SCXRD analysis. Figure 2 and Table S1 display the crystal structure and data of **NTTA-1**, respectively.

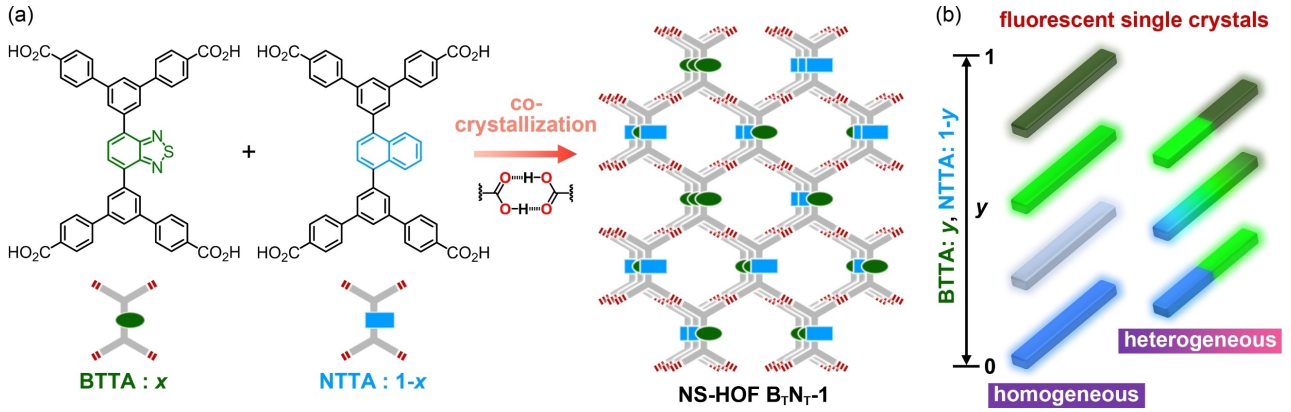

Figure 1. Single crystalline non-stoichiometric hydrogen-bonded organic frameworks (NS-HOFs) with rich fluorecence behaviors depending on composition ratios and distributions. (a) Construction of NS-HOF $\mathbf{B_TN_T}$**-1** composed of two different fluorescent tetracarboxylic acids with benzothiadiazole and naphthalene cores (**BTTA** and **NTTA** respectively) through complementary H-bonding. (b) Schematic representation of single crystals of $\mathbf{B_TN_T}$**-1** showing various homogeneous and heterogeneous fluorecence colors depending on composition ratios and distributions of two components. The observed fluorescence behaviors are unique to non-stoichiometric co-crystalline systems.

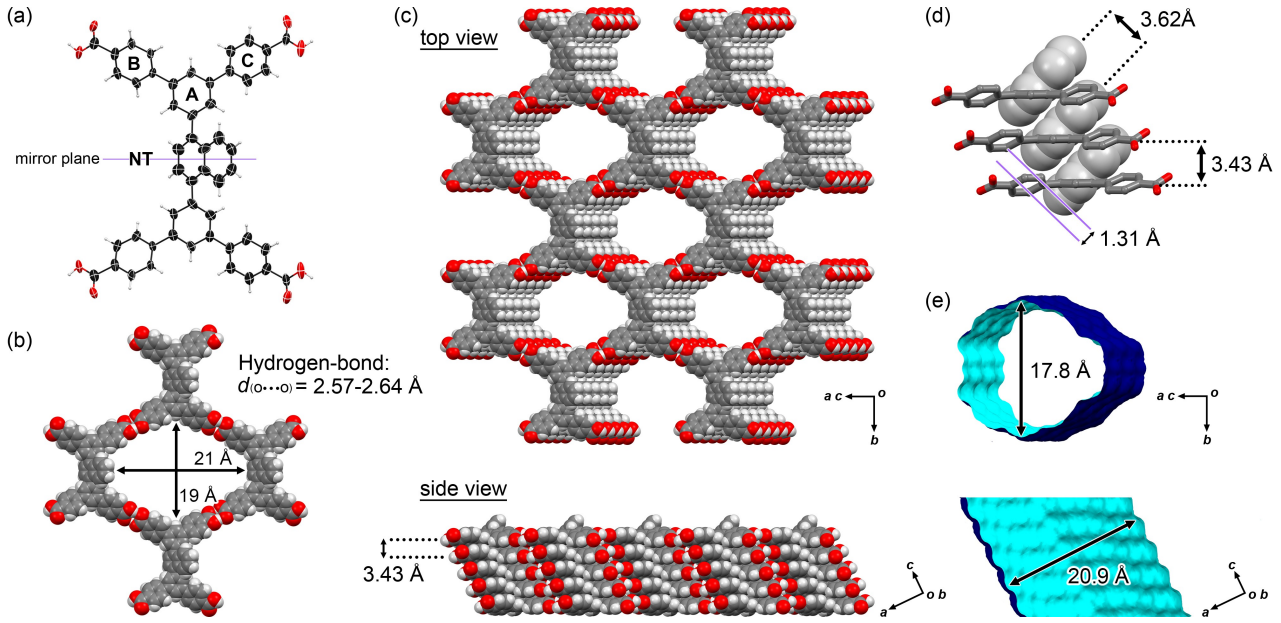

Figure 2. Crystal structure of **NTTA-1**. (a) Anisotropic displacement ellipsoid plot of **NTTA** with 50% probability. (b) Rhombic motif of a H-bonded network. (c) Packing diagrams. (d) Relative orientation of the stacking molecules, in which naphthalene moieties are drown by the space-fill models. (e) Visualized surface of 1D pore. The channels accommodate solvent molecules of TCB, which were only partially solved due to severe disorder.

NTTA-1, belonging to the space group *Cm*, has the isostructural framework with **BTTA-1**. A C_S-symmetric molecule of **NTTA** has a mirror plane perpendicular to the central NT ring. The NT ring is twisted from the neighboring benzene rings: A dihedral angle between the NT and benzene ring A [ω(NT–A)] is 46.7°. Dihedral angles between benzene rings A and B [ω(A–B)] and A and C [ω(A–C)] are 29.4° and 23.3°, respectively (Figures 2a and S2a). Carboxy groups of **NTTA** form self-complementary H-bonded dimers with O···O distances of 2.57–2.64 Å to give a ***sql***-topological 2D network sheet possessing rhombic pores with a size of 19 Å×21 Å (Figure 2b). The sheets are slip-stacked along the *c*-axis with an interlayer distance of 3.43 Å to give a porous framework possessing 1D channels, whose rhombic aperture has a dimension of 17.8 Å×20.9 Å (Figures 2c, and 2e). Molecules of TCB used as a recrystallization solvent are accommodated in the channel but some of them were not solved crystallographically due to severe disorder (Figure S2b). The NT moieties are unidirectionally slip-stacked through π–π interactions. The intermolecular distance between the NT moieties is 3.62 Å, and the stacked NT moiety is slipped by 1.31 Å along the direction parallel to the arrangement of NT (Figure 2d).

Crystallography of NS-HOF B_TN_T-1(x, y)

NTTA and **BTTA** were concurrently dissolved in a solution of DMF and TCB with various composition ratios. The solution was left at 100 °C to slowly evaporate the solvent, giving single crystals of NS-HOF $\mathbf{B_TN_T}$**-1**(x, y), where x and y denote the molar fraction of **BTTA**, i.e. $N_{\mathbf{BTTA}}$ / ($N_{\mathbf{BTTA}}$ + $N_{\mathbf{NTTA}}$), in the initially-prepared solution and crystallographically-determined occupancy of **BTTA** in the resultant single crystal, respectively. The NS-HOF whose y has not been determined is simply presented by $\mathbf{B_TN_T}$**-1**(x). The crystal structures were solved using a disorder model of **NTTA** and **BTTA**, and the composition ratio in single crystals was determined by optimizing their chemical occupancies during structural refinements.[32]

As a representative example, Figure 3 and Table S1 show the crystal structure and data of $\mathbf{B_TN_T}$**-1**(0.3, 0.395), respectively. Although $\mathbf{B_TN_T}$**-1**(0.3, 0.395) belongs to the space group *C*2/*m*, which is different from that of **BTTA-1** and **NTTA-1**, the crystal structure is basically similar to those of **BTTA-1** and **NTTA-1**, except for having an additional two-fold axis. The lattice parameters showed intermediate values between those of **BTTA-1** and **NTTA-1** except for the *b* axis. The core part of the molecule in $\mathbf{B_TN_T}$**-1**(0.3, 0.395) involves both BT and NT with optimized chemical occupancy of 0.395 and 0.605, respectively, indicating formation of a NS-HOF (Figure 3a). Compared to the mono-component HOFs, the core part in $\mathbf{B_TN_T}$**-1** is further disordered in two parts with opposite orientations related by the two-fold axis operation. Because of the disorders, the molecular structure has C_{2h}-symmetry. Molecular components connected by self-complementary H-bonds of the peripheral carboxy groups with O···O distances of 2.62 Å give a 2D networked sheet possessing rhombic pores with a size of 18 Å×23 Å (Figure 3b). The sheets are slip-stacked along the *c*-axis with an interlayer distance of 3.44 Å to give a porous framework possessing 1D channels that have smooth surface on the inside of the wall and an aperture with a dimension of 18.5 Å×19.4 Å (Figures 3c and 3e).

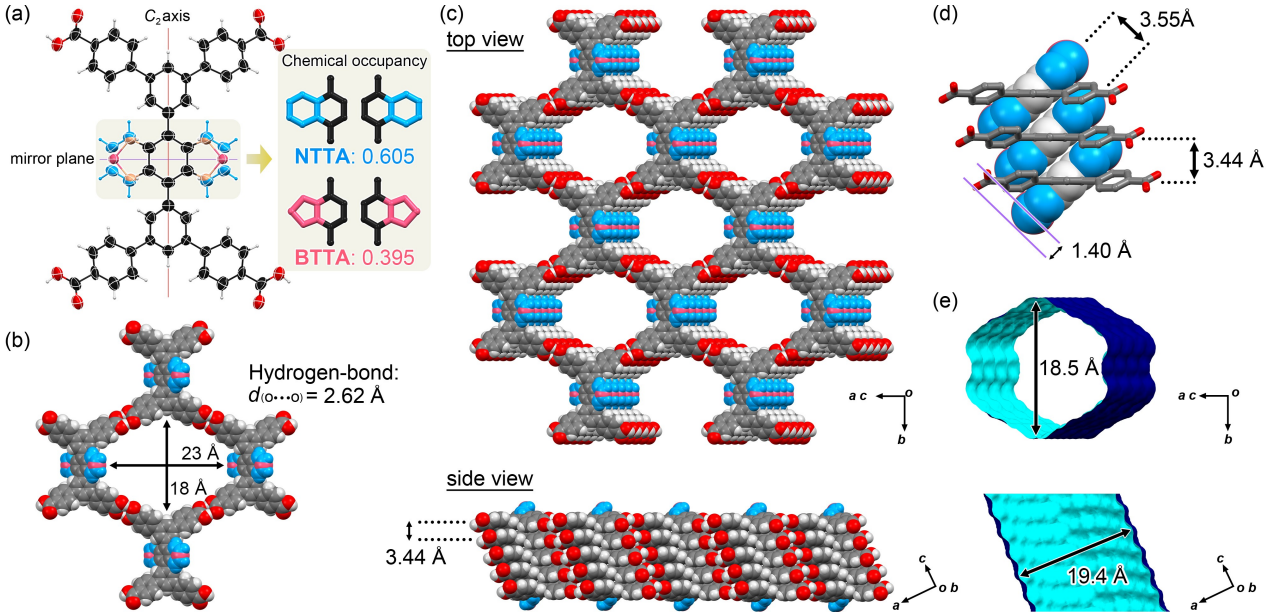

Figure 3. Crystal structure of $\mathbf{B_TN_T}$**-1** (a) Anisotropic displacement ellipsoid plot of $\mathbf{B_TN_T}$**-1** (0.3, 0.395) with 50% probability, in which the core moieties are disordered in two structures corresponding to **BTTA** and **NTTA**, with occupancies of 0.395 and 0.605, respectively. (b) Rhombic motif of a H-bonded network. (c) Packing diagrams. (d) Relative orientation of the stacking molecules, in which core moieties are drown by the space-fill models. (e) Visualized surface of 1D pore. The channels accommodate solvent molecules of TCB, which were not solved due to severe disorder.

Molecules of TCB used in the recrystallization are accommodated in the channel (not solved crystallographically due to severe disorder). The core moieties are slip-stacked by π–π interactions. The intermolecular distance between the core moieties is 3.55 Å, which is an intermediate value between that of **NTTA-1** and **BTTA-1**. The stacked core moiety is slipped by 1.40 Å along the direction parallel to the arrangement of cores (Figure 3d).

Crystallographic analyses were conducted on a total of 12 single crystals of $\mathbf{B_TN_T}$**-1** obtained from solutions with various composition ratios. Figure S3 and Table S2 give detailed crystal structures and data, respectively. Figure 4 shows the relation between the molar fraction (x) of **BTTA** in the initial solution and the chemical occupancy (y) of **BTTA** in the resultant single crystal of HOF $\mathbf{B_TN_T}$**-1**. If the components are statistically mixed to give crystals, values of x and y should be proportional as in the case of NS-HOFs **CP-HpPy-1** previously reported.[32] However, the present system shows no proportional relation between the x and y values, rather showing a sigmoidal curve. This trend is likely due to the much lower solubility of **BTTA** compared with that of **NTTA**: their solubility in DMF at 30 °C was determined to be 16.2 and 255 mmol L^{-1}, respectively. Moreover, the variation of y values with respect to the same x values is significant. For example, solutions with $x = 0.3$ resulted in crystals with y values ranging from 0.1 to 0.6.

The cell parameters for single crystals of $\mathbf{B_TN_T}$**-1**(x, y) have intermediate values between those of **BTTA-1** and **NTTA-1** and are approximately related to the y value (Figure 5). The lengths of the a, b axes and β angle of the unit cell increase from 28.4786(13) Å to 29.8700(6) Å, from 34.358(3) Å to 34.7553(7) Å and from 91.687(5)° to 97.792-

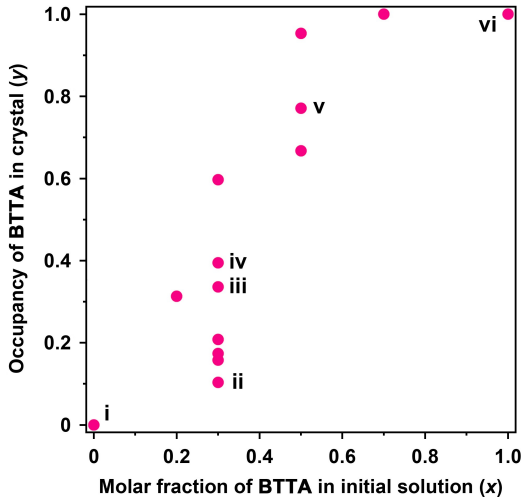

Figure 4. Composition in single-crystals of $\mathbf{B_TN_T}$**-1**(x, y), where x and y denote the molar fraction and occupancy of **BTTA** in the initial solution and the resultant single crystal, respectively. Single crystals with Roman numerals were also subjected to fluorescence microscope observation as shown in Figure 7b.

(2)°, respectively, as y value increases from 0 to 1 (Figures 5a, 5b, 5d). Similarly, the length of the c axis decreases from 3.8505(2) Å to 3.71190(10) Å (Figure 5c). The unit-cell volume V does not show clear correlation (Figure 5e). The distance between the two stacked central cores also decreases as the y value increases (Figure 5f). When y is 0 (i.e., **NTTA-1**), the distance between the stacked NT moieties is 3.63 Å. On the other hand, when y is 1 (i.e., **BTTA-1**), the corresponding distance between the

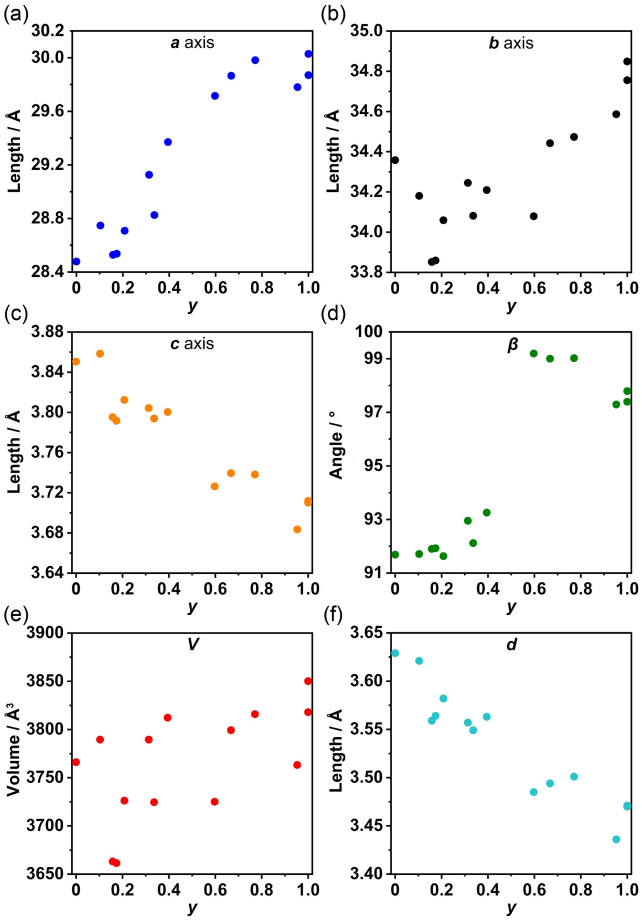

Figure 5. Crystallographic parameters for $\mathbf{B_TN_T}$**-1** with various *y* values: (a) *a* axis, (b) *b* axis, (c) *c* axis, (d) angle β, (e) cell volume *V*, and (f) intermolecular distance between central benzene cores *d*.

BT moieties is 3.47 Å. The single crystals of $\mathbf{B_TN_T}$**-1**(*x*, *y*) have a weighted average structure of **BTTA-1** and **NTTA-1**.

Stacking Interaction Energy

To consider favorable stacking manners of **BTTA** and **NTTA** moieties in $\mathbf{B_TN_T}$**-1**, intermolecular interaction energy (E_{dimer}) was calculated on homo-dimers (**BTTA/BTTA** and **NTTA/NTTA**) and hetero-dimer (**BTTA/NTTA**).[35,36] The dimer models were constructed based on the crystal structure of $\mathbf{B_TN_T}$**-1**(0.3, 0.395) that has an intermolecular distance of 3.490 Å. As Figure 3 shows, the disordered structure of $\mathbf{B_TN_T}$**-1** could contain totally nine kinds of stacking ways of the cores, which should be considered in the calculations. Parallel homo-stacking between **BTTA** cores and between **NTTA** ones gave two models: (1) **B/B**_para and (2) **N/N**_para, respectively. Antiparallel homo-stacking between **BTTA** cores and between **NTTA** cores gave the following four models: (3) **B/B**_anti_1, (4) **B/B**_anti_2, (5) **N/N**_anti_1, and (6) **N/N**_anti_2, where _1 and _2 denote two types of different stacking geometries derived from the disorder. Parallel hetero-stacking between **BTTA** and **NTTA** gave (7) **B/N**_para. Antiparallel hetero-stacking between **BTTA** and **NTTA** cores gave two models: (8) **B/N**_anti_1 and (9) **B/N**_anti_2. The structural details of the stacked dimer models are provided in Figures S4, S5.

The E_{dimer} value for each of the dimer models calculated at B97D/6-311+G(d,p) level of theory (Table S5). The averaged E_{dimer} values are summarized in Table 1. In both parallel and antiparallel stacked dimer models, the hetero-dimers have slightly larger E_{dimer} values than those of homodimers.

Thermal Stability and Porosity

The bulk crystalline samples of **NTTA-1**, **BTTA-1** and $\mathbf{B_TN_T}$**-1**(0.5) were subjected to thermal gravimetric (TG) analysis. The TG curve of **NTTA-1** reaches a plateau at ca. 207 °C with weight loss of 60 %, which indicates that the framework contains TCB molecules with a host/guest molar ratio of 1/6 (Figure S6). $\mathbf{B_TN_T}$**-1**(0.5) also showed 60 % weight loss until the solvent was completely removed at 195 °C (Figure S7). These behaviors are similar to that of **BTTA-1** previously reported (Figure S8).

HOFs **NTTA-1**, **BTTA-1** and $\mathbf{B_TN_T}$**-1**(0.5) were activated at 130 °C under vacuum conditions. **BTTA-1** remained in its original structure after removing the guest molecules to give activated HOF **BTTA-1a** as we reported.[33] We also confirmed, by PXRD measurements, that **NTTA-1** and $\mathbf{B_TN_T}$**-1**(0.5) retain their frameworks to give activated HOFs **NTTA-1a** and $\mathbf{B_TN_T}$**-1a**(0.5), respectively (Figures S9–S11). **BTTA-1a**, **NTTA-1a** and $\mathbf{B_TN_T}$**-1a**(0.5) were subject to N_2, O_2 and CO_2 sorption experiments at 77 K and 195 K, respectively (Figure 6). N_2 and O_2 sorption isotherms show rapid rise at low pressures and can be categorized in a type I isotherm, although they have a small step at $P/P_0 = 0.03$ for all samples (Figure 6a, 6b). A similar step at low pressure is often observed in HOFs with a large aperture of the pore size.[37,38] This is likely because the monolayer of adsorbed N_2 is fully formed before the pore finally filled.[39] The uptakes increase with increasing the composition of **BTTA** in the bulk crystals (Figure 6a, 6b). Brunauer–Emmett–Teller (BET) surface area of **BTTA-1a**, **NTTA-1a** and $\mathbf{B_TN_T}$**-1a**(0.5) was calculated to be 1560 $m^2 g^{-1}$, 628 $m^2 g^{-1}$ and 1111 $m^2 g^{-1}$, respectively, based on the N_2 sorption experiment (Figure S12, S14, S16). This indicates that the HOF containing more **BTTA** has larger BET surface area. This might be attributed to the difference in the interaction

Table 1: Averaged interaction energies (kcal mol^{-1}) for the stacked two molecules in anti or parallel arrangements.

Dimer model	E_{dimer}/kcal mol^{-1}
B/B_para	−41.08
B/B_anti	−41.12
N/N_para	−41.62
N/N_anti	−40.83
B/N_para	−42.47
B/N_anti	−41.23

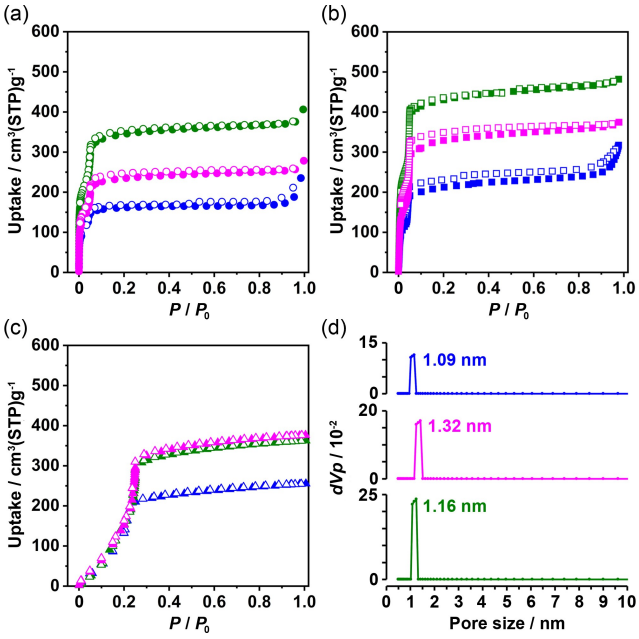

Figure 6. Gas sorption isotherms of the activated HOFs **NTTA-1a** (blue), **B_TN_T-1a**(0.5) (pink) and **BTTA-1a** (green) for (a) N_2 at 77 K, (b) O_2 at 77 K and (c) CO_2 at 195 K. Solid and open symbols correspond to adsorption and desorption processes, respectively. (d) NLDFT plots.

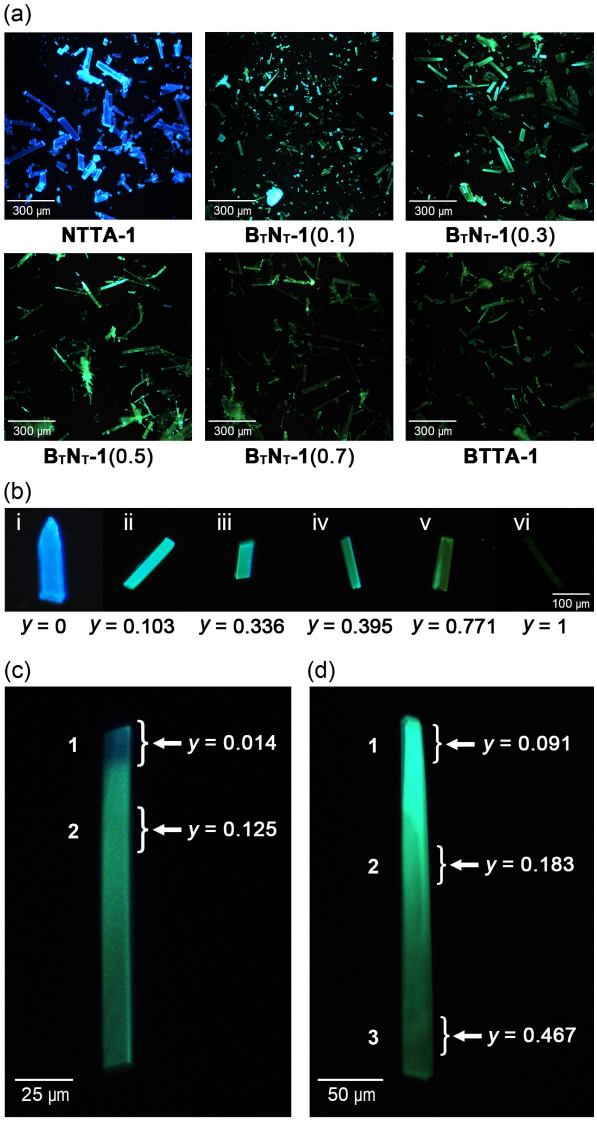

Figure 7. (a) Fluorescence photographs of bulk crystals of **NTTA-1**, **BTTA-1**, and **B_TN_T-1**(x) (x = 0.1, 0.3, 0.5, 0.7) HOFs, where x values show the molar fraction of **BTTA** in the initial solution. (b) Fluorescence photographs of single crystals whose composition ratios were determined by SCXRD. (c, d) Determination of composition ratio for several position in inhomogeneous single crystals showing (c) blue-green and (d) light green-dark yellow by local SCXRD analysis. y denotes the crystallographically-determined occupancy of **BTTA**.

of **BTTA** and **NTTA** with N_2 molecules or to difference in the crystallinity of the HOFs. Nonlocal density functional theory (NLDFT) calculations indicate that **BTTA-1a**, **NTTA-1a** and **B_TN_T-1a**(0.5) have the pore width of 11.6 Å, 10.9 Å and 13.2 Å, respectively (Figures 6d, S13, S15, S17). On the other hand, CO_2 sorption experiments show absorption isotherms with a gradual slope at pressures lower than P_e/P_0 = ca. 0.2 for all samples (Figure 6c) due to a smaller attractive interaction between a CO_2 molecule and the framework than that between CO_2 molecules, which is also often observed for HOFs with a large aperture of the pore.[37,38] The CO_2 uptakes of **BTTA-1a** and **B_TN_T-1a**(0.5) were nearly the same and higher than that of **NTTA-1a** (Figure 6c).

Fluorescence Colors of Single Crystals

In the following, we unravel the fluorescence behavior of HOFs **B_TN_T-1**. Clearly, the fluorescence colors of single crystals strongly depend on the molecular components, and therefore, can report on the distribution and fraction of the components in the single crystals. Figure 7a shows representative fluorescence photographs of bulk crystals of HOFs **NTTA-1**, **BTTA-1**, and **B_TN_T-1**(x) (x = 0.1, 0.3, 0.5, 0.7). The fluorescence color ranges from blue to dark yellow via green upon increasing the x value. Interestingly, we noticed that even in the same crystallization batch with a certain x value, crystals of **B_TN_T-1**(x) with different emission colors, such as blue and green, were formed. Furthermore, single crystals showing different fluorescence colors in different parts of the single crystal were concomitantly formed in the same batch. The distribution of the two components on the single crystal was successfully visualized to be either homogeneous or heterogeneous.

Figure 7b shows photographs of some single crystals' emission and their chemical occupancy of **BTTA** (y), which were determined by SCXRD analysis. Each of the crystals corresponds to a point denoted by the same Roman numeral in Figure 4. The fluorescence color ranges from blue to dark yellow via light green upon increasing the chemical occupancy (y) in the crystal.

Furthermore, we conducted local X-ray diffraction analysis at a couple of points on single crystals showing inhomogeneous blue-green or light green-dark yellow fluorescence colors (Figures 7c, 7d, Table S3, S4). The result reveals the relationship between the crystal structures, composition ratios, and fluorescence colors, depending on the position on the crystal. A synchrotron X-ray beam focused on a surface of a diameter of approximately 1 μm was used for the exploration. The molecular packings were the same for all positions, whereas the composition ratios vary at each position. As Figure 7c shows, an edge part in blue color contains small amount of **BTTA** ($y = 0.014$), while the light green one next to the edge contains about 10 % of **BTTA** ($y = 0.125$). Similarly, another crystal has a **BTTA** occupancy of 0.091, 0.183, and 0.467 at a light-green edge, a green middle part, and a dark yellow edge, respectively. These results clearly unravel that the inhomogeneous distribution of the components forming single crystals of **B_TN_T-1** HOF makes the fluorescence properties more versatile.

Emission Spectra of NTTA-1, BTTA-1, and B_TN_T-1 Single Crystals under the Microscope

To shed more light on the local fluorescence behavior of single crystals of NS-HOF **B_TN_T-1**, we performed fluorescence microscopy experiments. The excitation wavelength was 371 nm for all the measurements using crystals of **NTTA-1**, **BTTA-1** and **B_TN_T-1**. Figure 8 shows representative photographs of excited single crystals, and their emission spectra recorded from different points on the crystal. To begin with, Figure 8a shows the emission spectra of **NTTA-1** single crystal (crystal-A) collected from various local positions. Two observations to highlight: (1) the spectra exhibit a band profile with three peaks at around 435, 525 and 570 nm; and (2) the emission intensity of the spectrum depends on the interrogated zone, most probably due to the interrogated surface being close to or far from the focal point at each observation region. Notice that this dependence is not due a quenching process as the emission decays have the same profile giving the same lifetime values (Table S6). The most intense band at 435 nm is attributed to

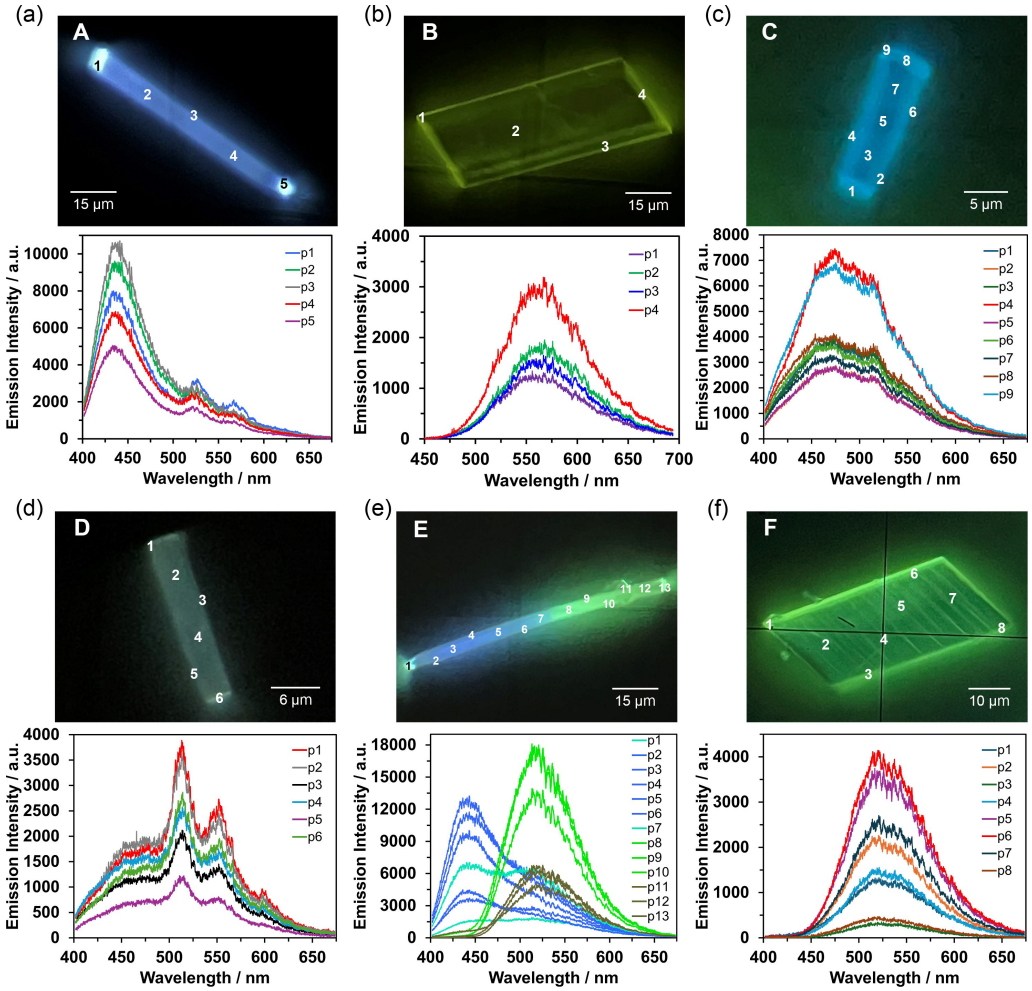

Figure 8. Emission photographs and spectra obtained of representative single crystals of the synthesized and studied HOFs: (a) **NTTA-1**, (b) **BTTA-1** and (c to f) **B_TN_T-1**(0.3): blue (crystal-C), white (crystal-D), blue-green (crystal-E) and green (crystal-F). The points on the crystal indicate the position from where the emission spectra were recorded.

the emission from excited **NTTA** monomers. The other bands are assigned to excited dimers or oligomers derived from unidirectional stacking of the NT moieties in the crystal. These oriented molecular structures at the excited states might lead to the formation of excimers by interaction of stacked monomers at ground and excited states or formation of anionic species upon interaction of two carboxylic groups of neighboring **NTTA** molecules.[40,41] Note that the emission spectrum of amorphous solid of **NTTA** (**NTTA**-Amor) in which the molecules are randomly oriented does not show the 525 and 570 nm bands (Figure S18).

Figure 8b shows that the emission spectra of a **BTTA-1** single crystal (crystal-B) exhibit a broad band (full width at half maximum, FWHM $\approx$ 3000 cm^{-1}) at around 560 nm, and their intensity depends on the interrogated zone. The largely Stokes-shifted green-yellow emission band suggests the occurrence of an excited-state charge-transfer reaction in the molecules. We notice that the emission intensity maxima of both **NTTA-1** and **BTTA-1** are red-shifted by 20–30 nm compared with those of the amorphous solids, **NTTA**-Amor and **BTTA**-Amor, respectively (Figure S19). The emission redshift is due to stacking of the molecules in the HOFs, allowing π–π interaction in the framework and stabilization of the excited monomers. Figure S20 and S21 show various examples of images and spectra of **NTTA-1** and **BTTA-1**.

In the following, we focus on understanding the NS-HOFs photobehaviors under the microscope. We selected four single crystals of $\mathbf{B_TN_T}$**-1**(0.3) covering the typical fluorescence behaviors of this batch (Figure 8c–8f). Interestingly, under UV light, the photographs of single crystals exhibit different emission colors: blue (crystal-C), white (crystal-D), blue-green (crystal-E) and green (crystal-F), with varying levels of heterogeneous distributions. The recorded fluorescence spectra at several positions on each crystal present a rich and complex behavior, not only from crystal to crystal in the same batch, but also on a single and same crystal. Additionally, we explored the photobehavior of several crystals of $\mathbf{B_TN_T}$**-1** prepared with different mixing ratios of the components ($x = 0.1$–0.9) (Figure S22).

As previously commented, the two molecular components forming $\mathbf{B_TN_T}$**-1** crystals allow the observation of different emission spectra depending on the molar fraction and their distribution in the crystal (Figures 8c–8f). Taking as an example the results using the $\mathbf{B_TN_T}$**-1**(0.3) batch and the studied crystals, we can classify them in four types: (1) crystal-C that shows a broad band around 475 nm with shoulders at 515 and 550 nm (Figure 8c), (2) crystal-D, which exhibits a band around 470 nm with two intense peaks at 515 and 550 nm (Figure 8d), (3) crystal-E that shows spectra having two different and separated emission bands with intensity maxima at 440 and 525 nm (Figure 8e), and (4) crystal-F exhibiting a broad and single emission band with its intensity maximum at 525 nm (Figure 8f), reminiscent of the green band for crystal-E. The spectral profiles recorded at different positions on the single crystal are very similar, except for those of crystal-E, although their intensities depend on the interrogated point. This suggests a homogeneous distribution of the two components (**NTTA** and **BTTA**) forming these $\mathbf{B_TN_T}$**-1** selected single crystal.

Based on the discussion of the emission bands of **NTTA-1** and **BTTA-1**, we assign the emission of the crystals-C and -D at around 475 nm to excited **NTTA** monomers, while the emission at 515–550 nm reflects overlapping emission bands from excimers/anions of the **NTTA** moieties and **BTTA** monomers (Figures 8 and S23). The significant decrease in the emission from excited **NTTA** monomer (~435 nm) observed in crystals-C, -D and -F, and the spectral overlap between the emission of **NTTA**-Amor and absorption of **BTTA**-Amor suggests that an energy transfer likely happens from **NTTA** to the neighboring molecules of **BTTA** (Figures S19, Figure 8c, 8d, 8f).

Emission Decays and Anisotropy of NTTA-1, BTTA-1 and B_TN_T-1 HOFs Single Crystals under the Micro-Scope

To investigate the excited species giving rise to the emissions observed from each single crystal, fluorescence decay curves were recorded for **NTTA-1**, **BTTA-1** and $\mathbf{B_TN_T}$**-1**(0.3) crystals-C, -D, -E, and -F. We used two optical filters to specifically select and monitor the emissions of **NTTA-1** in the 420–470 nm range (Detection in region 1, D1) and of **BTTA-1** in the 560–610 nm one (Detection in region 2, D2). Figure 9 shows selected emission decays of **NTTA-1, BTTA-1** and examples of mixed HOFs, while Figures S24–S29 give additional examples of decays from selected points on different crystals. All the signals exhibit complex behaviors with a bi- or triexponential decay. Considering that complexity, the large amount of recorded and analyzed data, and aiming to simplify the picture, we grouped in Table 2 the obtained data from the best fits of the decays, from an analysis depending on the emission color of the crystal. While Tables S6–S13 give more details on the values of the emission lifetimes, depending on the emission color and the used ratio to synthesize the mixed HOF.

To begin with the decays of **NTTA-1**, the fits of the signals collected at D1 give time constants of $\tau_1 = 1.0$–1.5, $\tau_2 = 2.9$–4.2 and $\tau_3 = 6.5$–9.7 ns, while those at D2 give 0.7–2.0 and 7.0–8.9 ns (Tables 2 and S6). In the latter, the short lifetime corresponds to a rising component which value depends on the selected crystal and interrogated point. We believe that the decaying signals at D1 and D2 regions reflect the same channel, connecting the emissions of the linkers ($\tau_2 = 2.9$–4.2 ns) and of formed excimers or proton-transfer ones (7.0–8.9 ns).

The signals collected at the single yellow emission band of **BTTA-1** crystals decay biexponentially with time constants, $\tau_1 = 0.7$–0.9 and $\tau_2 = 2.5$–4.4 ns, with the short component being the main one (Tables S7). In this case, we did not observe any rising component within our time resolution limit (about 200 ps). We suggest that the short component reflects the emission decay of the excited **BTTA** molecules, while the longest one is of formed charge-transfer species, photoproduced in a time shorter than 200 ps.

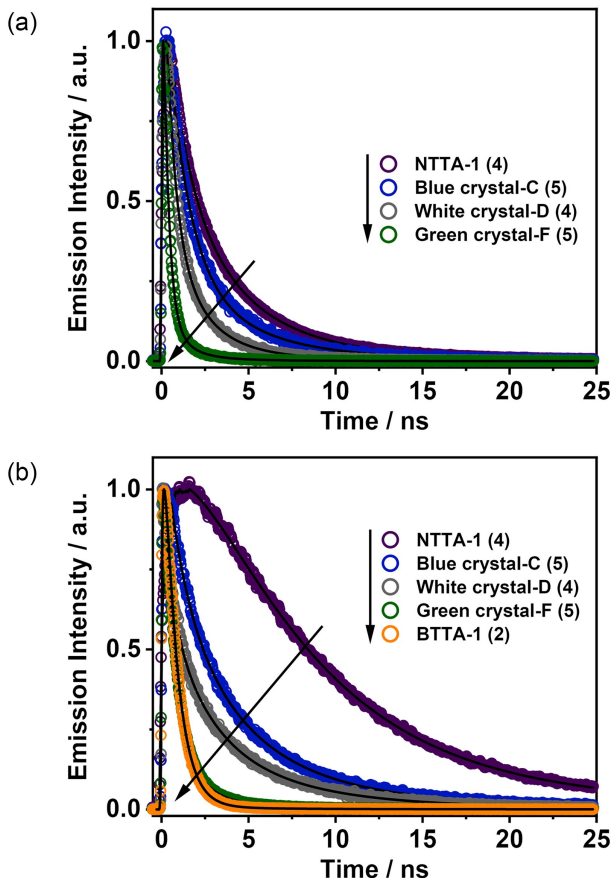

Figure 9. Fluorescence emission decays of excited single crystals of **NTTA-1**, **BTTA-1** and **B_TN_T-1** (crystals-C, -D and -F) shown in Figure 8. The signal was monitored using two different filters: (a) Detected region 1 (D1) and (b) detected region 2 (D2). The solid lines are from the best fits using a multiexponential function. The number in brackets indicates the interrogated point on the crystal shown in Figure 8.

Now, we focus on the emission decays of the mixed crystals. Figure 9 shows decays of selected **B_TN_T-1**(0.3) single crystals gated at D1 and D2, and Figures S26–S29 give more examples including those gated from different zones of the crystals. Tables S8–S13 exhibit the obtained time constants from the best multiexponential fits. Although the behavior is complex, a trend depending on the emission color of the **B_TN_T-1** mixed crystals can be observed. From blue to greenish yellow emission color single crystals, the emission decays at D1 spectral region (420–470 nm) were fitted using three exponential functions with time constants: $\tau_1 = 0.2–1.1$, $\tau_2 = 1.0–3.8$ and $\tau_3 = 2.9–8.4$ ns, while for those gated at D2 (560–610 nm), the best fits give: $\tau_1 = 0.3–2.7$, $\tau_2 = 0.8–5.3$ and $\tau_3 = 3.6–12.0$ ns. We first notice that, as Figure 8 suggests, the recorded decays at D1 spectral region are coming from the **NTTA-1** component in the NS-HOF. However, we observe that the values of the lifetimes at D1 for the NS-HOFs are shorter than those observed for **NTTA-1** ones. This shortening in the lifetimes value suggests a photo-induced interaction between neighboring molecules of **NTTA** and **BTTA**. Such interaction could be brought about by an energy-transfer from the former to the latter molecules, as suggested by the overlap between their respective emission (donor) and absorption (acceptor) spectra (Figure S19). Energy-transfer has been suggested to occur in mixed MOFs and HOFs.[16–18,31] At D2 region, both partners in the single crystals emit, and we cannot provide a reasonable picture from the obtained lifetimes. These must reflect a combined and complex photo-behavior involving emission decays of several species, dynamics of excimer formation, energy-, proton- and charge-transfer events at the excited states. Notice the heterogeneity of the formed crystals and the different profiles of the emission decays and spectra gated from the same crystal. Due to these competing fast decays and rising events, contrary to the behavior of **NTTA-1** at D2 region, we could not observe any rising component at D2 of the mixed crystals.

We also explored the emission anisotropy behavior of selected single crystals of **NTTA-1**, **BTTA-1** and **B_TN_T-1**(0.3). All the crystals studied show anisotropic emission behaviors that also depend on the crystal orientation (Figure 10). Similar strong anisotropic behavior has been reported for other HOF materials.[42,43,44] The strongest anisotropy dependence on the crystal orientation is observed for **BTTA-1** (Figure 10a) showing distributions centered on −0.1 (vertical orientation) and 0.8 (horizontal orientation). Although the **NTTA-1** fluorescence anisotropy (Figure 10b) is less influenced by the crystal orientation, the dependence shows the opposite trend in

Table 2: Range of the lifetime values (τ_i) obtained from the fits of the emission decays (at spectral regions D1 and D2) of the single crystals of the studied HOFs. The values were grouped according to the emission color of the crystals and considering the data in Table S12.

HOF sample	Color	Spectral Region D1 (420–470 nm)			Spectral Region D2 (560–610 nm)		
		τ_1/ns	τ_2/ns	τ_3/ns	τ_1/ns	τ_2/ns	τ_3/ns
NTTA-1	Blue	1.0–1.5	2.9–4.2	6.5–9.7	0.7–2.0[a]	-	7.0–8.9
BTTA-1	Yellow	–	–	–	0.7–0.9	2.5–4.4	–
B_TN_T-1	Blue	0.2–1.1	1.3–3.8	3.3–8.4	0.6–1.4	1.7–5.2	4.0–9.7
	Green	0.2–0.7	1.3–3.6	4.0–7.0	0.6–1.6	1.9–4.5	6.4–10.0
	Yellow	–	–	–	0.3–0.9	0.8–5.3	3.7–7.9
	White	0.5–0.6	1.6–1.9	3.7–5.5	0.4–0.9	1.4–3.2	5.6–6.8
	Blue-Green	0.5–0.6	1.3–2.5	3.3–7.2	0.8.1.5	2.1–4.5	5.4–12.0
	Green-Yellow	0.3–0.8	1.0–2.4	2.9–6.0	0.6–2.7	1.3–5.3	3.6–9.2

[a] Indicates a rising component in the emission signal.

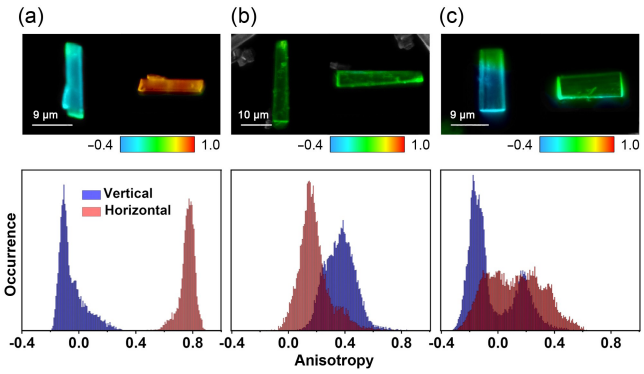

Figure 10. Representative fluorescence anisotropy images and histograms obtained from single crystals of (a) **BTTA-1**, (b) **NTTA-1**, and (c) **B_TN_T-1**(0.3).

comparison to **BTTA-1**. For **NTTA-1**, the perpendicular crystal orientation produces a histogram centered on higher anisotropy values (0.4), while the histogram for the horizontal orientation is centered on 0.1. The difference in the emission anisotropy behavior between the **NTTA-1** and **BTTA-1**, having similar crystal structure, indicates disparity in the emission dipole moment orientation for these crystals and might be associated with differences in the interactions between the respective molecular units. Finally, in agreement with the structural and photophysical properties of the **B_TN_T-1**(0.3) mixed crystals, the anisotropy value distributions are broad and span from −0.2 to 0.4 with only a slight dependence on the crystal orientation. The observed emission anisotropy behavior further supports the ordered crystalline structure of the samples studied.

As observed in the PXRD experiments on **NTTA-1**, **BTTA-1** and **B_TN_T-1** HOFs, their frameworks remain the same after removing the guest solvent molecules (Figures S9–S11). We also explored whether the guest solvent used in the crystallization influences the photobehavior of the NS-HOFs, by recording fluorescence lifetime images (FLIM), emission spectra and lifetime decays of three selected crystals of **B_TN_T-1**(0.3), before and after desolvation (upon heating for 3 h at 130 °C, under a vacuum condition). Figure S30 shows no significant changes in the photobehavior upon desolvation of these blue, blue-green and green emitting crystals and interrogated at different sites. Therefore, desolvation of these HOFs under vacuum does not affect the framework structure nor their photobehavior, which indicates the robustness of these materials.

Conclusions

In this contribution, we report on the synthesis, characterization, and photobehavior of single crystalline, NS-HOFs (**B_TN_T-1**) composed of **NTTA** and **BTTA**, and their parent mono-component frameworks (**NTTA-1** and **BTTA-1**). SCXRD analysis revealed that **B_TN_T-1** has isostructural frameworks with that of the parent HOFs, and that **NTTA** and **BTTA** can be non-stoichiometrically mixed in the framework with diverse components ratios and distribution manners. The heterogeneous distribution of the components was thoroughly confirmed by focused synchrotron X-ray diffraction and time-resolved fluorescence microscopy analyses on single crystals of **B_TN_T-1**. Remarkably, the rich fluorescence behavior of **B_TN_T-1** depends on the composition ratio and distribution of the components in the single crystals. Indeed, we observed not only fluorescence bands of various colors, such as uniform monocolors of purple, blue, white, green and yellow, but also different emission bands and colors from a single crystal. We provide details on their emission lifetimes and discuss their origins following the composition, emission color and targeted region on the interrogated single crystal.

These results demonstrate unique optical properties can be achieved using single crystalline NS-HOFs, and therefore, NS-HOFs are a promising candidate for new smart functional porous materials. To get a highly homogeneous or heterogeneous distribution of the two components in the **B_TN_T-1** selectively, one has to explore the effect of solvent nature, the temperature and the time of precipitation on the distribution in single crystals. We are planning to perform these experiments in near future.

Supporting Information

Supporting Information is available from the Wiley OnlineLibrary. CCDC Nos. 2388166 for **NTTA-1**, 2388167 for **B_TN_T-1**(0.3,0.395), 2388168 for **B_TN_T-1**(0.2, 0.313), 2388169 for **B_TN_T-1**(0.3, 0.103), 2388170 for **B_TN_T-1**(0.3, 0.158), 2388171 for **B_TN_T-1**(0.3, 0.174), 2388172 for **B_TN_T-1**(0.3, 0.208), 2388173 for **B_TN_T-1**(0.3, 0.336), 2388174 for **B_TN_T-1**(0.3, 0.597), 2388175 for **B_TN_T-1**(0.5, 0.667), 2388176 for **B_TN_T-1**(0.5, 0.771), 2388177 for **B_TN_T-1**(0.5, 0.953), 2388178 for **B_TN_T-1**(0.7, 1.000), 2388179 for **B_TN_T-1**(0.3, 0.014), 2388180 for **B_TN_T-1**(0.3, 0.125), 2388181 for **B_TN_T-1**(0.3, 0.091), 2388182 for **B_TN_T-1**(0.3, 0.183), and 2388183 for **B_TN_T-1**(0.3, 0.467) contain the supplementary crystallographic data for this paper. These data are provided free of charge by the joint Cambridge Crystallographic Data Centre and Fachinformationszentrum Karlsruhe.

Acknowledgements

This work was supported by KAKENHI (JP23H04029, JP24K21769, JP24K01468, JP24H00405 and JP24K21717) from JSPS and MEXT Japan, and by grant PID2020-116519RB-I00 funded by MICIU/AEI/10.13039/501100011033 and the European Union (EU), SBPLY/23/180225/000196 funded by JCCM and the EU through "Fondo Europeo de Desarrollo Regional" (FEDER); grant 2022-GRIN-34325 funded by UCLM (FEDER).

T. H. thanks financial support by Grant-in-Aid for JSPS Research Fellow (JP24KJ1655). M.H. thanks MICIU for the FPI fellowship PRE2021-099064 financed by MICIU/AEI/10.13059/501100011033 and by FSE+. I. H. thanks Hoansha Foundation and the Multidisciplinary Research Laboratory System for Future Developments (MRL), Graduate School of Engineering Science, Osaka University for their financial support. The authors thank the Cybermedia Center, Osaka University, for use of the Super-computer for Quest to Unsolved Interdisciplinary Datascience (SQUID). The authors acknowledge Ms. R. Miyake at Osaka University for HR-MS analysis. Synchrotron X-ray diffraction data were collected at BL40XU at SPring-8 with approval of the Japan Synchrotron Radiation Research Institute (JASRI, proposal Nos. 2023A1264, 2024A1208, and 2024B1717). Dr. K. Ichiyanagi and Dr. T. Sasaki are acknowledged for synchrotron radiation experiments. The authors deeply appreciate the reviewers for fruitful comments.

Conflict of Interest

The authors declare no conflict of interest.

Data Availability Statement

The data that support the findings of this study are available in the supplementary material of this article.

Keywords: Nonstoichiometric crystal · co-crystal · hydrogen-bonded organic framework · multicolor emission · fluorescence microscopy

[1] H. Furukawa, U. Müller, O. M. Yaghi, *Angew. Chem. Int. Ed.* **2015**, *54*, 3417–3430.
[2] S. P. Teong, Y. Zhang, *ChemNanoMat* **2023**, *9*, e202300263.
[3] S. J. Lee, S. G. Telfer, *Angew. Chem. Int. Ed.* **2023**, *62*, e202306341; *Angew. Chem.* **2023**, *135*, e202306341.
[4] R. L. Li, A. Yang, N. C. Flanders, M. T. Yeung, D. T. Sheppard, W. R. Dichtel, *J. Am. Chem. Soc.* **2021**, *143*, 7081–7087.
[5] M. Wang, T. Zeng, Y. Yu, X. Wang, Y. Zhao, H. Xi, Y.-B. Zhang, *J. Am. Chem. Soc.* **2024**, *146*, 1035–1041.
[6] V. Guillerm, D. Kim, J. F. Eubank, R. Luebke, X. Liu, K. Adil, M. S. Lah, M. Eddaoudi, *Chem. Soc. Rev.* **2014**, *43*, 6141–6172.
[7] S. Yuan, L. Feng, K. Wang, J. Pang, M. Bosch, C. Lollar, Y. Sun, J. Qin, X. Yang, P. Zhang, Q. Wang, L. Zou, Y. Zhang, L. Zhang, Y. Fang, J. Li, H.-C. Zhou, *Adv. Mater.* **2018**, *30*, 1704303.
[8] J.-R. Li, J. Sculley, H.-C. Zhou, *Chem. Rev.* **2012**, *112*, 869–932.
[9] V. F. Yusuf, N. I. Malek, S. K. Kailasa, *ACS Omega* **2022**, *7*, 44507–44531.
[10] H. Deng, C. J. Doonan, H. Furukawa, R. B. Ferreira, J. Towne, C. B. Knobler, B. Wang, O. M. Yaghi, *Science* **2010**, *327*, 846–850.
[11] W. J. Newsome, S. Ayad, J. Cordova, E. W. Reinheimer, A. D. Campiglia, J. K. Harper, K. Hanson, F. J. Uribe-Romo, *J. Am. Chem. Soc.* **2019**, *141*, 11298–11303.
[12] J. Perego, C. X. Bezuidenhout, I. Villa, F. Cova, R. Crapanzano, I. Frank, F. Pagano, N. Kratochwill, E. Auffray, S. Bracco, A. Vedda, C. Dujardin, P. E. Sozzani, F. Meinardi, A. Comotti, A. Monguzzi, *Nat. Commun.* **2022**, *13*, 3504.
[13] J. Y. Choi, M. Wang, B. Check, M. Stodolka, K. Tayman, S. Sharma, J. Park, *Small* **2023**, *19*, 2206988.
[14] C. Schlüsener, M. Xhinovci, S.-J. Ernst, A. Schmitz, N. Tannert, C. Janiak, *Chem. Mater.* **2019**, *31*, 4051–4062.
[15] K. C. Park, C. Seo, G. Gupta, J. Kim, C. Y. Lee, *ACS Appl. Mater. Interfaces* **2017**, *9*, 38670–38677.
[16] J. Jia, L. Gutiérrez-Arzaluz, O. Shekhah, N. Alsadun, J. Czaban-Jóźwiak, S. Zhou, O. M. Bakr, O. F. Mohammed, M. Eddaoudi, *J. Am. Chem. Soc.* **2020**, *142*, 8580–8584.
[17] M. Orfano, J. Perego, C. X. Bezuidenhout, I. Villa, R. Lorenzi, B. Sabot, S. Pierre, S. Bracco, S. Piva, A. Comotti, A. Monguzzi, *Adv. Funct. Mater.* **2024**, *34*, 2404480.
[18] M. Gutiérrez, F. Sánchez, A. Douhal, *Chem. Eur. J.* **2016**, *22*, 13072–13082.
[19] R. L. Li, A. Yang, N. C. Flanders, M. T. Yeung, D. T. Sheppard, W. R. Dichtel, *J. Am. Chem. Soc.* **2021**, *143*, 7081–7087.
[20] W. Zhao, C. Yu, J. Zhao, F. Chen, X. Guan, H. Li, B. Tang, G. Yu, V. Valtchev, Y. Yan, S. Qiu, Q. Fang, *Small* **2021**, *17*, 2102630.
[21] B. Gui, X. Liu, Y. Cheng, Y. Zhang, P. Chen, M. He, J. Sun, C. Wang, *Angew. Chem. Int. Ed.* **2022**, *61*, e202113852; *Angew. Chem.* **2022**, *134*, e202113852.
[22] M. Wang, T. Zeng, Y. Yu, X. Wang, Y. Zhao, H. Xi, Y.-B. Zhang, *J. Am. Chem. Soc.* **2024**, *146*, 1035–1041.
[23] Y. He, S. Xiang, B. Chen, *J. Am. Chem. Soc.* **2011**, *133*, 14570–14573.
[24] R.-B. Lin, Y. He, P. Li, H. Wang, W. Zhou, B. Chen, *Soc. Rev.* **2019**, *48*, 1362–1389.
[25] I. Hisaki, C. Xin, K. Takahashi, T. Nakamura, *Angew. Chem. Int. Ed.* **2019**, *58*, 11160–11170; *Angew. Chem.* **2019**, *131*, 11278–11288.
[26] B. Wang, R.-B. Lin, Z. Zhang, S. Xiang, B. Chen, *J. Am. Chem. Soc.* **2020**, *142*, 14399–14416.
[27] X. Song, Y. Wang, C. Wang, D. Wang, G. Zhuang, K. O. Kirlikovali, P. Li, O. K. Farha, *J. Am. Chem. Soc.* **2022**, *144*, 10663–10687.
[28] P. Li, M. R. Ryder, J. F. Stoddart, *Acc. Mater. Res.* **2020**, *1*, 77–87.
[29] T. Miyano, I. Hisaki, N. Tohnai, *Chem. Lett.* **2017**, *46*, 225–227.
[30] X. Yu Gao, Y. Wang, E. Wu, C. Wang, B. Li, Y. Zhou, B. Chen, P. Li, *Angew. Chem. Int. Ed.* **2023**, *62*, e202312393; *Angew. Chem.* **2023**, *135*, e202312393.
[31] Q. Chen, T. Zhang, X. Chen, M. Liang, H. Zhao, P. Yuan, Y. Han, C.-P. Li, J. Hao, P. Xue, *ACS Appl. Mater. Interfaces* **2022**, *14*, 24509–24517.
[32] T. Hashimoto, R. Oketani, M. Nobuoka, S. Seki, I. Hisaki, *Angew. Chem. Int. Ed.* **2023**, *62*, e202215836; *Angew. Chem.* **2023**, *135*, e202215836.
[33] Z. Yang, A. Saeki, A. Inoue, R. Oketani, K. Kamiya, S. Nakanishi, T. Nakamura, I. Hisaki, *Cryst. Growth Des.* **2022**, *22*, 4472–4479.
[34] D. Ren, H.-L. Xia, K. Zhou, S. Wu, X.-Y. Liu, X. Wang, J. Li, *Angew. Chem. Int. Ed.* **2021**, *60*, 25048–25054; *Angew. Chem.* **2021**, *133*, 25252–25258.
[35] S. Tsuzuki, K. Honda, T. Uchimaru, M. Mikami, K. Tanabe, *J. Am. Chem. Soc.* **2000**, *122*, 3746–3753.
[36] S. Tsuzuki, K. Honda, T. Uchimaru, M. Mikami, K. Tanabe, *J. Am. Chem. Soc.* **2002**, *124*, 104–112.
[37] B. Wang, X.-L. Lv, J. Lv, L. Ma, R.-B. Lin, H. Cui, J. Zhang, Z. Zhang, S. Xiang, B. Chen, *Chem. Commun.* **2020**, *56*, 66–69.

[38] Y. Suzuki, M. Gutiérrez, S. Tanaka, E. Gomez, N. Tohnai, N. Yasuda, N. Matubayasi, A. Douhal, I. Hisaki, *Chem. Sci.* **2021**, *12*, 9607–9618.
[39] K. S. Walton, R. Q. Snurr, *J. Am. Chem. Soc.* **2007**, *129*, 8552–8556.
[40] M. R. di Nunzio, I. Hisaki, A. Douhal, *J. Photochem. Photobiol., C: Photochem. Rev.* **2021**, *47*, 100418.
[41] M. De La Hoz Tomás, J. Á. Organero, M. R. Di Nunzio, T. Hashimoto, I. Hisaki, A. Douhal, *J. Mater. Chem. C.* **2024**, *12*, 9112–9129.
[42] M. R. di Nunzio, E. Caballero-Mancebo, B. Cohen, A. Douhal, *J. Photochem. Photobiol., C: Photochem. Rev.* **2020**, *44*, 100355.
[43] I. Hisaki, N. Ikenaka, E. Gomez, B. Cohen, N. Tohnai, A. Douhal, *Chem. Eur. J.* **2017**, *23*, 11611–11619.
[44] I. Hisaki, Y. Suzuki, E. Gomez, B. Cohen, N. Tohnai, A. Douhal, *Angew. Chem. Int. Ed.* **2018**, *57*, 12650–12655; *Angew. Chem.* **2018**, *130*, 12832–12837.

Manuscript received: October 16, 2024
Accepted manuscript online: November 25, 2024
Version of record online: ■■, ■■

Research Article

Organic Materials

T. Hashimoto, M. d. l. Hoz Tomás, R. Oketani, B. Cohen, M. Naruoka, N. Tohnai, A. Douhal,* I. Hisaki* e202419992

Single Crystalline, Non-Stoichiometric Hydrogen-Bonded Organic Frameworks Showing Versatile Fluorescence Depending on Composition Ratios and Distributions

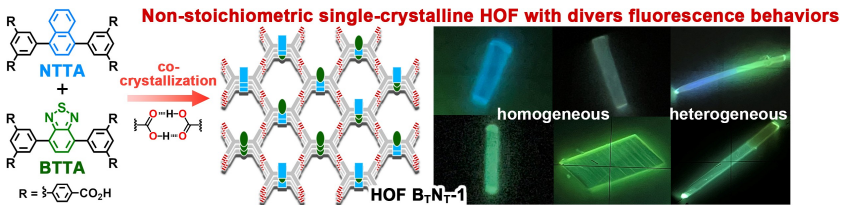

Homogeneous and heterogeneous fluorescence with versatile colors were achieved on single crystals of non-stoichiometrically mixed bicomponent hydrogen-bonded organic frameworks with permanent porosity. Focused synchrotron X-ray diffraction analysis and microscopic fluorescence spectroscopy on single crystals reveal structure and property relationship.